Energetics of internal tides around the Kerguelen Plateau from modeling and altimetry

Claire Maraldi, Florent Lyard, Laurent Testut, Richard Coleman

Energetics of internal tides around the Kerguelen Plateau from modeling and altimetry

Claire Maraldi,[1,2] Florent Lyard,[1] Laurent Testut,[1] and Richard Coleman[3,4]

Received 16 July 2010; revised 28 January 2011; accepted 9 February 2011; published 14 June 2011.

[1] A barotropic tidal model, with a parameterization term to account for the internal wave drag energy dissipation, is used to examine areas of possible M_2 internal tide generation in the Kerguelen Plateau region. Barotropic energy flux and a distribution of wave drag dissipation are computed. The results suggest important conversion of barotropic energy into baroclinic tide generation over the northern Kerguelen Plateau shelf break, consistent with a theoretical criterion based on ocean stratification, tidal forcing frequency, and bathymetric gradients. The sea surface height signatures of time-coherent internal tides are studied using TOPEX/Poseidon and Jason-1 altimeter data, whose ascending tracks cross nearly perpendicular to the eastern and western Kerguelen Plateau shelf break. Oscillations of a few centimeters associated with phase-locked internal tides propagate away from the plateau over distances of several hundred kilometers with a ~110 km wavelength. When reaching the frontal area of the Antarctic Circumpolar Current, the internal tide cannot be identified because of the aliasing of mesoscale variability into the same alias band as M_2. Finally, using altimeter data, we estimate the M_2 barotropic tidal power converted through the internal tide generation process. We find consistent values with the barotropic model parameterization estimation, which is also in good agreement with global internal tide model estimates. Combined with modeling, this study has shown that altimetry can be used to estimate internal tide dissipation.

Citation: Maraldi, C., F. Lyard, L. Testut, and R. Coleman (2011), Energetics of internal tides around the Kerguelen Plateau from modeling and altimetry, *J. Geophys. Res.*, *116*, C06004, doi:10.1029/2010JC006515.

1. Introduction

[2] The barotropic tides in the ocean are generated from astronomical forces (lunar-solar) with horizontal tidal currents that are nearly uniform in the vertical throughout the water column. The generation of internal tides results from the interaction between the barotropic tidal currents and strong bathymetric gradients. This leads to vertical displacements of the isopycnals at the same barotropic tide forcing frequency [*Siedler and Paul*, 1991; *Vlasenko and Morozov*, 1993; *Dushaw et al.*, 1995].

[3] Typical values of pycnocline displacement due to internal tides are of the order of 10 m, but they can reach larger values. *Chiswell* [1994] has observed amplitudes of 15 m in the region just north of the Hawaiian Islands and *Pingree and New* [1989] have observed displacements larger than 200 m in the Bay of Biscay. However, sea surface height signatures of internal tides are only a small fraction of pycnocline displacements, being scaled by the reduced gravity $g' = g\Delta\rho/\rho$ (g is the gravity, ρ is the density), typically of the order of 10^{-3} [*Apel*, 1987]. Thus, owing to the reduced gravity effects, sea surface internal tide amplitudes are only a few centimeters. However, previous studies have shown that high-precision altimetry can be used to observe time-coherent (e.g., phase-locked) internal tides [*Kantha and Tierney*, 1997; *Ray and Mitchum*, 1996, 1997; *Cummins et al.*, 2001].

[4] Studies using altimetry at the global scale have already put forward the hypothesis of internal tide signals in the Kerguelen Plateau (KP) region (see Figure 1 and *Kantha and Tierney* [1997] and *Carrère et al.* [2004]). These observations have also been corroborated with global internal tide models [*Morozov*, 1995; *Simmons et al.*, 2004].

[5] In this paper we use a barotropic tide model using a parameterization term to account for the internal wave drag energy dissipation [*Maraldi et al.*, 2007] and a theoretical criterion [*Baines*, 1986] to determine regions of internal tide generation in the KP region. We then analyze the sea surface height signals recorded by the TOPEX/Poseidon (TP) and Jason-1 satellite radar altimeters. The study is limited to the semidiurnal M_2 tidal component which is dominant in the region. Using these results, we examine the energetics of the M_2 internal tide for the first baroclinic mode and compare it with other estimations.

2. Areas of Internal Tide Generation

[6] Internal tide generation is possible in areas with strong bathymetric gradients, cross-slope flow of barotropic tidal

[1]Laboratoire d'Etudes en Géophysique et Océanographie Spatiales, CNRS, Toulouse, France.
[2]Now at Service Hydrographique et Océanographique de la Marine, Toulouse, France.
[3]Antarctic Climate and Ecosystems CRC, Hobart, Australia.
[4]Institute for Marine and Antarctic Studies, University of Tasmania, Hobart, Tasmania, Australia.

0148-0227/11/2010JC006515

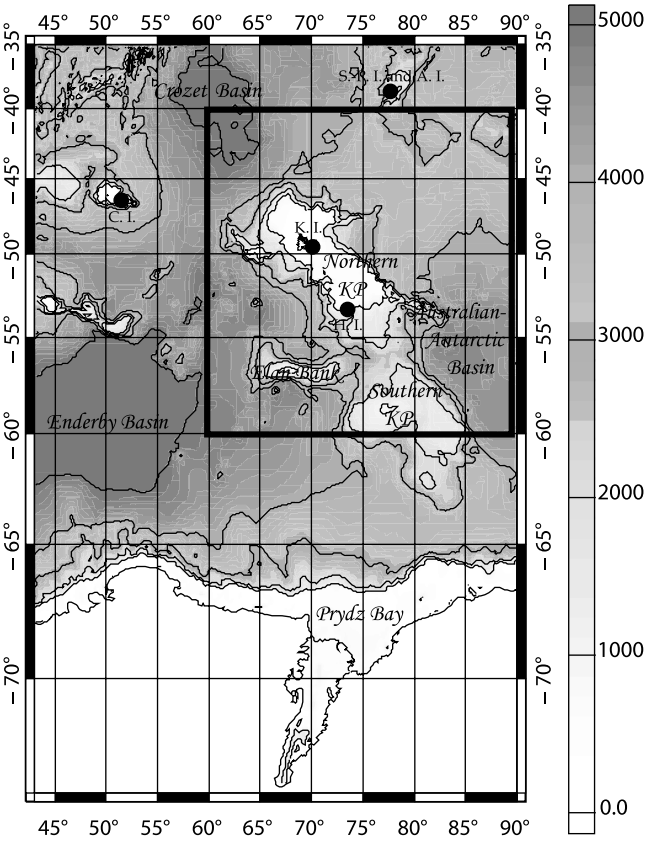

Figure 1. Bathymetry (in m) of the Southern Indian Ocean. The black dots correspond to the Kerguelen Islands (K. I.), Crozet Island (C. I.), Saint-Paul and Amsterdam Islands (S.-P. I. and A. I.), and Heard Island (H. I.). The box corresponds to the region of study. The bathymetry contours at every 1000 m are overplotted.

currents and a stratified water column. Thus, barotropic tide models can help us to characterize the sites of internal tide generation along the KP shelf break. We use the *T-UGO-m* (*MOG2D* follow-on; see http://sirocco.omp.obs-mip.fr/eng/tools/Tugo/Home/TugoHome.htm) model to compute barotropic tides in the southern Indian Ocean. This nonlinear, time stepping model computes the sea level variations and currents due to tidal forcing by solving the momentum and shallow water equations on a finite element mesh. The space discretization method allows the mesh to be larger in the deep ocean and the resolution can be increased in coastal regions and regions with strong bathymetric gradients, enabling sufficient resolution for gravity waves: the grid mesh size ranges from a few kilometers or less along the coastlines and the KP slope, to about 100 km in the deep ocean. The tidal model has been run over a 1 year period so that each tidal component could be well separated when using harmonic analysis. Our model solved five semidiurnal (M_2, S_2, K_2, N_2, $2N_2$), four diurnal (K_1, O_1, P_1, Q_1) and three long-period (M_m, M_f, M_{tm}) tidal constituents with tidal elevations prescribed at the open boundaries using the FES2004 solution [*Lyard et al.*, 2006]. The elevations of the model have been validated against in situ data, including tide gauges, pelagic moorings and GPS buoys, and altimeter data at crossover points [*Maraldi et al.*, 2007] giving us confidence in the model tidal solution (Figure 2).

[7] The study of tidal ellipses over ocean shelf break regions and areas with strong bathymetric gradients is useful to determine internal tide generation sites. The M_2 tidal ellipses from the barotropic tide model are represented in Figure 3a. At the eastern and western slopes of the northern KP (Figure 1), tidal ellipses are quasi-perpendicular to the isobaths and their amplitudes, amplified over the plateau, are very large. As a consequence, these M_2 tidal currents are very likely to lead to internal tide generation. The mass flux and the mean energy flux due to M_2 tide propagation are also pertinent parameters to look at when searching for internal tide generation areas. Indeed, in two dimensional models of internal tides, the forcing is proportional to the cross-slope volume flux which is often the most important factor determining internal tide generation [*Baines*, 1982; *Morozov*, 1995; *Simmons et al.*, 2004]. For a given wave, the mean energy flux ($\vec{F}$) over a tidal period T can be written as follows:

$$\vec{F}(x,y) = \rho g h \frac{1}{T}\int_0^T \eta(x,y,t)\vec{u}(x,y,t)dt \qquad (1)$$

where ρ is the mean ocean density, g the gravitational acceleration, h the ocean depth, η the tidal surface elevation and $\vec{u}$ its depth-averaged current velocity. This flux is represented in Figure 3b for the M_2 constituent. Significant flux of tidal energy occurs over the KP from its eastern slope in a northeasterly direction. In particular, the model gives an estimate of total power of 97 GW crossing the plateau between Kerguelen Islands and Heard Island. On this basis we may expect that the northern KP is a likely site for the conversion of barotropic tidal energy into baroclinic tides.

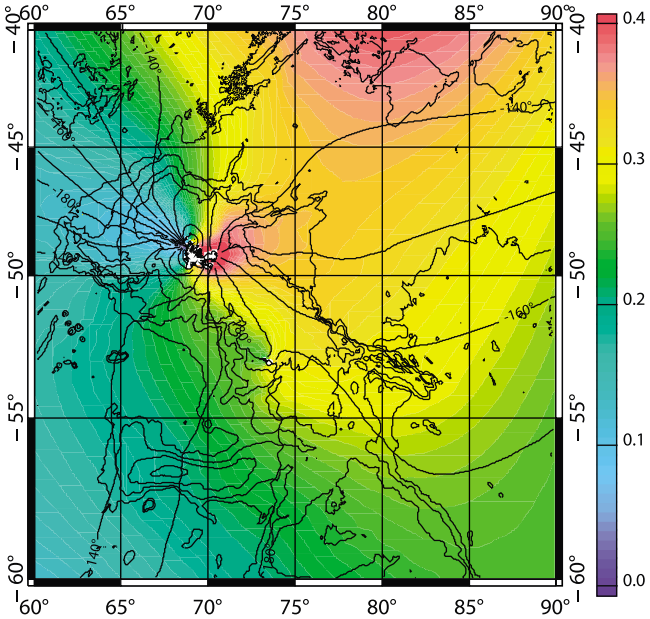

Figure 2. M_2 amplitudes in cm. M_2 tidal phase lines are presented. The bathymetry contours at every 1000 m are overplotted.

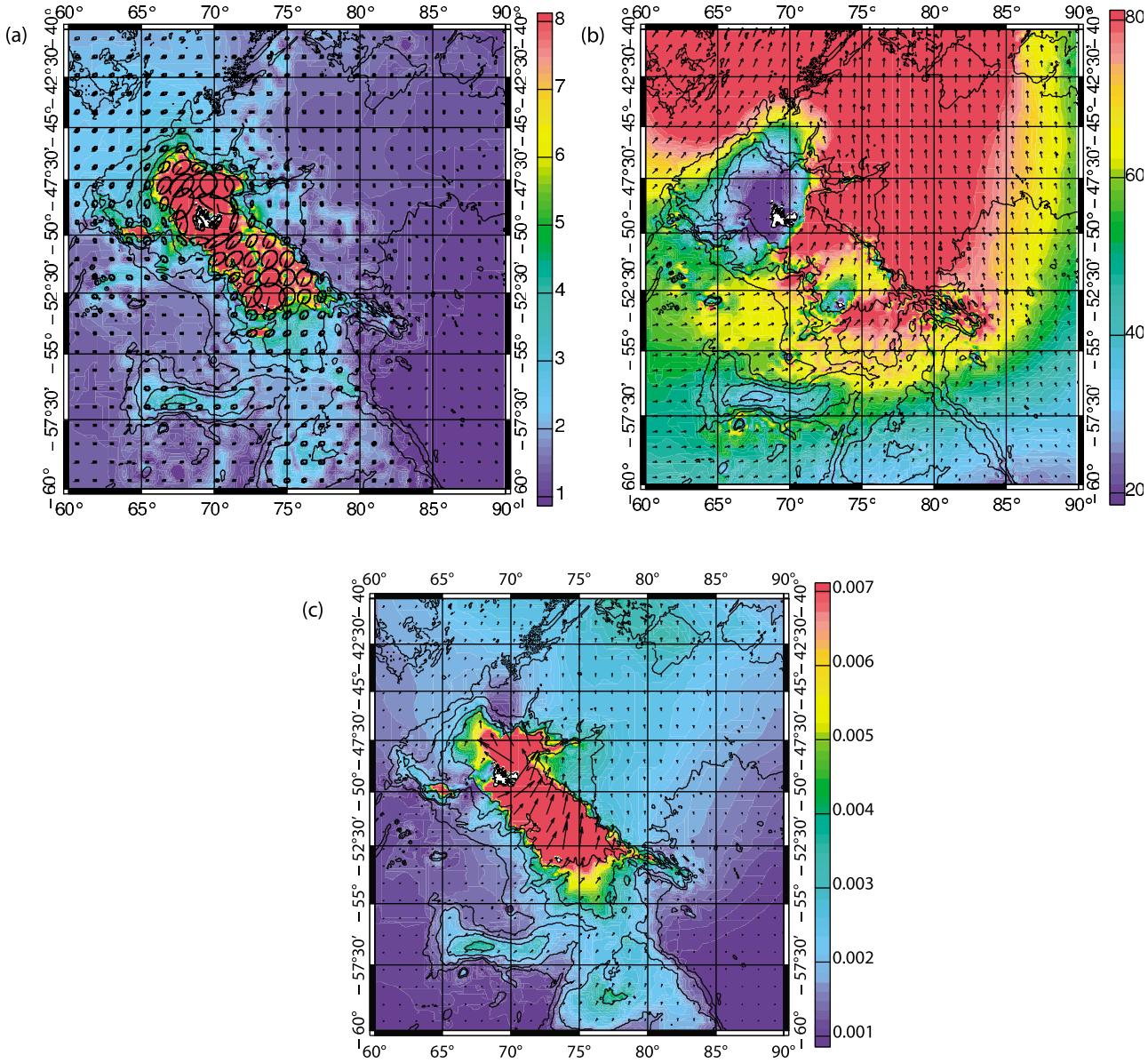

Figure 3. (a) M_2 tidal ellipses in cm s^{-1}. The lines from ellipse center indicate the phase. (b) M_2 barotropic depth-integrated energy flux in kW m^{-1}. (c) M_2 mass transport in m^{-2} s. The bathymetry contours at every 1000 m are overplotted.

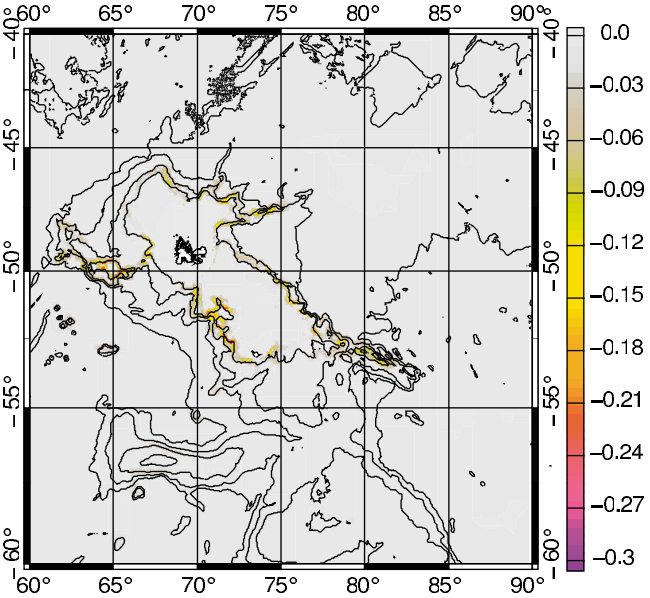

Figure 4. M_2 wave drag dissipation (W m^{-2}) obtained from the model parameterization term to account for the internal wave drag energy dissipation ($-\|\vec{D}\|$; see equation (2)). The bathymetry contours at every 1000 m are overplotted.

[8] One of the useful attributes of the *MOG2D/T-UGOm* model is the use of a dissipation term to account for the internal wave drag energy dissipation. Some parameterizations have already been proposed to take account of the internal wave drag in the case of typical horizontal length scales smaller than the local tidal excursion [*Jayne and St. Laurent*, 2001; *Llewellyn Smith and Young*, 2002; *Egbert et al.*, 2004]. These parameterizations are valid for topographic scales that are typically of the order of 1000 m and less. From altimetry observations, the main sources of internal waves are located on much larger topographic structures, such as volcanic ridges. That is also the case of the KP which extends for more than 2200 km in a northwest-southeast direction. The *T-UGOm* model uses an original parameterization which was designed to deal with large topographic scales [*Lyard et al.*, 2006]. The energy transfer from the barotropic to the baroclinic modes is parameterized as follows:

$$\vec{D} = C\rho\kappa^{-1}N\left(\vec{\nabla}H\vec{u}\right)\vec{\nabla}H \qquad (2)$$

where κ is the typical topography horizontal wave number, H is the ocean mean depth, N is a depth-weighted average buoyancy frequency, with weights decreasing linearly from the ocean bottom up to the surface to account for the vertical velocity upward linear profile [*Lyard et al.*, 2006] and C = 200 (dimensionless) is an empirical tuning coefficient. This dissipation term is applied for depths greater than 200 m. At shallower depths, the bottom friction dissipation mostly dominates and gives a good estimation of the barotropic energy dissipated. The parameterization of baroclinic energy generation in the FES2004 global tide model simulation leads to a globally integrated internal wave drag dissipation estimate of 0.7 TW for the M_2 component. This estimate is close to the *Egbert and Ray* [2001] value derived from altimeter

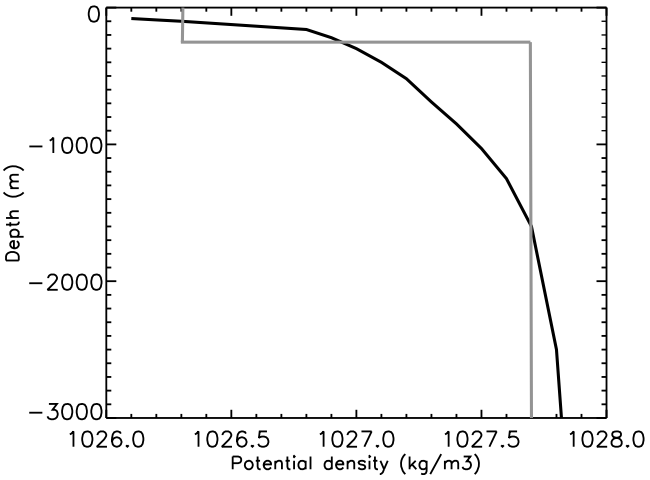

Figure 5. Potential density profile in the region east of the KP [from *Park et al.*, 1993]. The two-layer approximation potential density profile is added on the plot (gray lines).

data as the coefficient C in equation (2) has been empirically tuned to agree with this estimation. Figure 4 represents the M_2 wave drag dissipation from the regional model [*Maraldi et al.*, 2007] in the KP region. Over the northern part of the KP, the integrated M_2 energy dissipation from barotropic to baroclinic modes represents more than 2% of the global estimate. This result from our barotropic model indicates that there is a pronounced transfer from M_2 barotropic tide energy to M_2 baroclinic tide generation.

[9] Theoretical criteria can also indicate areas of internal tide generation. Two basic parameters control the dynamics of internal waves near bottom topographic features [*Vlasenko et al.*, 2005]. They are the inclination angle of internal wave propagation rays, denoted as α, which is the ratio between the

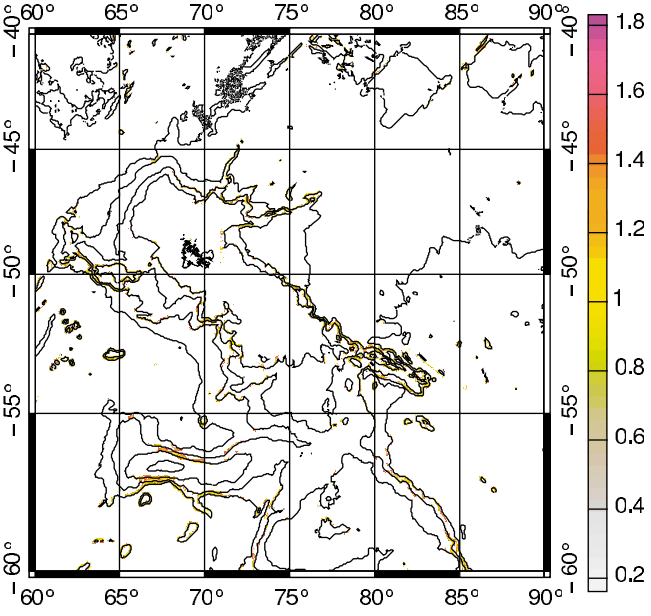

Figure 6. The γ criterion [*Baines*, 1986]. Colored areas ($\gamma \approx 1$) correspond to possible M_2 internal tide generation regions. The bathymetry contours at every 1000 m are overplotted.

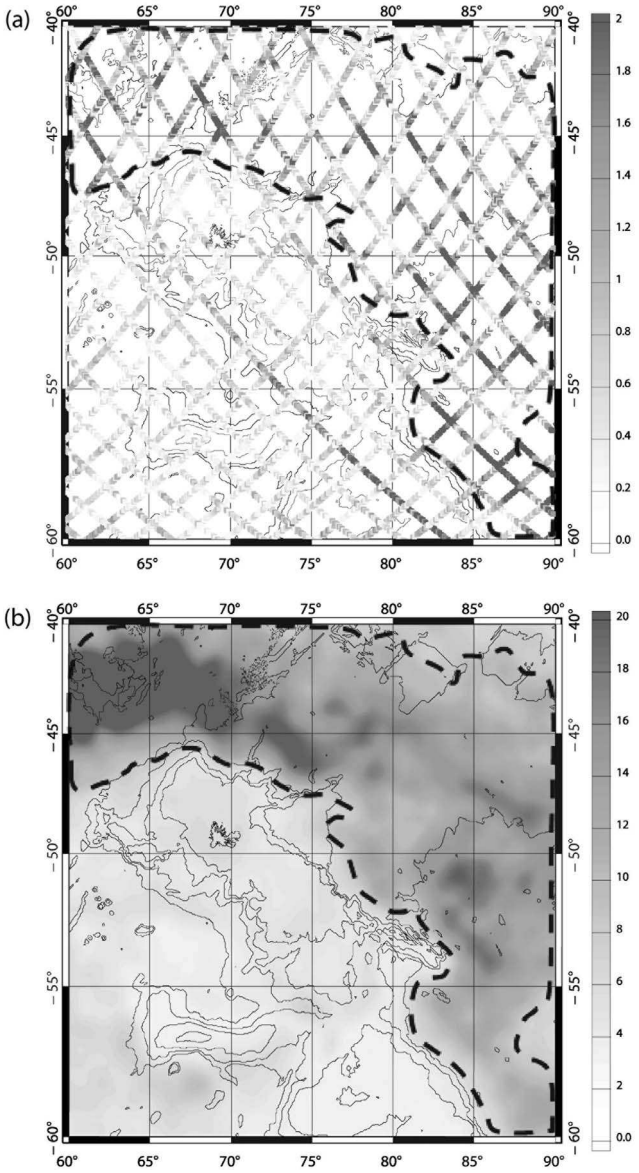

Figure 7. (a) RMS of the M_2 along-track amplitudes from TOPEX/Poseidon and Jason-1 altimetry (in cm). (b) RMS of the sea level anomalies (in cm) over the 1992–2006 period computed using the Archiving, Validation, and Interpretation of Satellite Oceanographic (AVISO) gridded product (www.aviso.oceanobs.com). This figure highlights the high mesoscale activity in the ACC area (dashed line).

frequency of the wave and the Brünt-Väisälä frequency (N), and the bathymetric gradient $\vec{\nabla}H$. The relationship between these two parameters is very important from the point of view of generation of internal waves. *Baines* [1986] proposed a formulation linking these two parameters, allowing a determination of the necessary conditions for internal wave generation. The Baines relation (γ) is dependent of the norm of the bathymetric gradient and of the inclination angle of internal wave propagation rays and is written in the form:

$$\gamma = \frac{\left\|\vec{\nabla}H\right\|}{\alpha} \tag{3}$$

When $\gamma \approx 1$, the inclination of the bottom topography is close to critical as it is nearly tangential to the characteristic lines of the wave equation [*Vlasenko et al.*, 2005]. The movement of the fluid is essentially baroclinic through the water column, and resonating phenomena induce a maximum of internal wave activity. The Brunt-Väisälä frequency was determined from the stratification according to the relation:

$$N = \sqrt{-\frac{g}{\rho_0}\frac{\partial \rho}{\partial z}} \tag{4}$$

with the gravitational acceleration $g = 9.8$ m s^{-2}, the mean density $\rho_0 = 1027.8$ kg m^{-3}, and the potential density profile computed in the region to the east of the KP using CTD sections made between the KP and Amsterdam Island (see *Park et al.* [1993] and Figure 5). We obtain a depth averaged value of $N = 0.002$ s^{-1}. Figure 6 represents the γ criterion [*Vlasenko et al.*, 2005] and supports the hypothesis of internal tide generation at the eastern and western shelf break of the northern KP.

3. Analysis of Altimeter Data

3.1. Method

[10] The baroclinic tide signal is composed of a component phase-locked to the barotropic tide and an incoherent residual component [*Mitchum and Chiswell*, 2000]. The phase-locked component has sufficient coherence in both time and space for its surface signal to be detected by TOPEX/Poseidon (TP) and Jason-1 altimeter data. Their orbit repeat period of 9.9156 days has been chosen specifically to resolve the major tidal harmonics over an expected mission lifetime [*Parke et al.*, 1987]. We used 10 years of TP data combined with 5 years of Jason-1 data, spanning the period from September 1992 to 2007. Along-track sea surface heights have been extracted using the X-TRACK data processing facility [*Roblou et al.*, 2006]. Thus, the time series are long enough to decouple the aliased M_2 period from the other major constituent periods according to the Rayleigh criterion. We applied standard instrumental and geophysical corrections to the altimeter records, including the barotropic response of the ocean to atmospheric pressure and wind forcing [*Carrère and Lyard*, 2003]. No ocean tide corrections were made. The 18.6 year lunar node tide variability, which can have effects of order of a few centimeters on the tidal constituents, was not taken into account. Instead, tidal constants for 20 constituents, including the main tidal constituents M_2, S_2, K_2, N_2, K_1, O_1, P_1, Q_1, were computed using a least squares harmonic analysis method applied to all repeats of the altimeter at each position along each track. As barotropic tides are mainly large-scale waves [*Ray and Mitchum*, 1996, 1997], we used a high-pass space filtering of along-track tidal constituents to remove the barotropic component in the sea surface signal. If A represents the amplitude of the tidal constituent and ϕ its phase, we have filtered $A\cos(\phi)$ and $A\sin(\phi)$ to separate the barotropic and the baroclinic components [*Dushaw*, 2002]. Around the KP, the first mode baroclinic wave speed is between 1.4 cm s^{-1} and 2.0 cm s^{-1} [*Chelton et al.*, 1998]. Accordingly, the wavelength of the first mode M_2 semidiurnal constituent is about 110 km. The TP ascending tracks are nearly perpendicular to the KP slope, but to take into

account the angle between TP tracks and internal tide propagation direction, we have applied a 200 km high-pass filter to the altimeter data. We have also smoothed the signals below 50 km to reduce the altimeter noise. This filtering is designed specifically to isolate the first mode of internal tides. The residual signal, obtained by taking the difference between the harmonic constants and the smoothed signal, is composed of the internal tide surface signature and noise. Indeed, the narrow-band filtering in both time and space retains the first mode baroclinic tide signal around the KP, but there is also a mesoscale signal in high-variability areas, such as the Antarctic Circumpolar Current region.

3.2. Limitation of the Method

[11] As noted by *Desai et al.* [1997] and *Tierney et al.* [1998], the oceanic general circulation is the principal source of error when computing the barotropic tides from altimetry. To investigate the barotropic M_2 variability, we have computed its amplitude and phase constituents over different periods: 1992–2008, 1992–2000, and 2000–2008. As the differences are mainly in the tidal amplitudes when evaluating the stability of the barotropic tides [*Carrère et al.*, 2004], we have computed the RMS of the M_2 along-track amplitudes for each of the three periods. From Figure 7, we do not see any significant temporal variability for the M_2-like signal amplitude on these multiyear time scales except in the Antarctic Circumpolar Current (ACC) area [*Park et al.*, 1998]. Over the ACC area, the RMS is larger than 2 cm. This is explained by the high level of nontidal signal in the altimeter signal due to ACC mesoscale activity, whose variability periods include the M_2 aliased period (62.1 days) for the TP and Jason-1 repeat period. Outside this ACC region, the RMS values are at the subcentimeter level. Some variability between the chosen time intervals may be barotropic changes associated with the 18.6 year lunar node tide variability but the results are fairly stable for the three subepochs, attesting to the stability in time of the M_2 along-track amplitudes.

4. Results

[12] We present results on Figure 8 for track 153 which crosses the KP at nearly right angles to the bathymetry contours (see Figure 9 for the location of track 153). At the east of the northern KP (i.e., north of 51°S for this track), the M_2 amplitudes show clear oscillations of a few centimeters. Several findings support our assertion that these oscillations are associated with a surface signature of internal tides propagating away from the northeastern KP shelf break.

[13] 1. In theory, internal tides are generated where there are strong topographic gradients. Here the oscillations appear at the edge of the KP shelf break and reduce in amplitude moving into deeper water.

[14] 2. As ascending track 153 crosses the east of the northern KP slope at approximately right angles, we can expect the M_2 internal tide to propagate almost in the same direction along the altimeter track, and thus two consecutive peaks give the approximate wavelength of the first M_2 baroclinic mode. By averaging from multiple peaks and multiple tracks, we find that the wave crests are separated by about 110 km distance which corresponds to the M_2 wavelength of the first baroclinic mode deduced from the first mode baroclinic wave speed [*Chelton et al.*, 1998].

[15] 3. The hypothesis is also corroborated by the M_2 phase of the residual signal. A wave propagating in a given x axis direction can be written as:

$$A_p \cos(\omega_p t - k_x x + \phi_p)$$

where A_p and ϕ_p are the amplitude and the phase of the wave, ω_p the frequency and k_x the wave number. Thus for a propagating wave, the phase constantly increases or decreases when propagating in the x direction. In our case, x is perpendicular to the KP slope and the phase of the internal tide propagating wave increases (decreases) with latitude when it propagates northward (southward). Figure 8b represents the phase of the residual signal. It indicates that the wave propagates away from the Kerguelen Plateau in the northward direction.

[16] We have thus demonstrated that the small oscillations being added and subtracted to the M_2 barotropic signal amplitudes correspond to a surface signature of the first mode of internal tides. However, this signature disappears after some three oscillations (i.e., a few hundred kilometers; see Figures 8a and 9) whereas studies in the Hawaii region have found M_2 baroclinic tide propagation over more than 1000 km [*Dushaw et al.*, 1995; *Ray and Mitchum*, 1996, 1997]. The phase of the residual signal also shows a break or discontinuity in the wave propagation at the same latitude (48°S) along track 153. This area corresponds to the southernmost extension of the ACC (Figure 7b), where the aliased period of the M_2 component is contained within the ACC mesoscale variability. The short-time Fourier transform supports this analysis (see Figure 8c). This method determines the along-track wavelengths contained in the baroclinic tide elevation signal. At the northeast shelf break, we see wavelengths around 110 km which disappear when arriving near the ACC.

[17] Figure 9 shows baroclinic tidal amplitudes along the ascending tracks crossing the KP. Tracks 77 and 153 indicate identical generation processes and a consistent propagation over a few hundred kilometers. They show small amplitudes after the slope and oscillate in a very correlated way before vanishing in the ACC area, where we mainly see nontidal signals due to the ACC mesoscale activity. In the southwest KP shelf break area, only track 1 has the characteristics of internal tides in both amplitude and phase propagation. After two oscillations, its surface signature disappears. A possible explanation for these decreasing amplitudes is an interference of the wave with other waves generated at the strong bathymetric gradient situated at 55°S. Another plausible reason for different internal tide characteristics in the southwest KP region is different stratification [*Park et al.*, 1998].

5. Energetics of the M_2 Baroclinic Tides

[18] The tide energy dissipated over the global ocean is about 3.7 TW, of which 2.5 TW is from the M_2 component [*Cartwright*, 1993; *Kagan and Sündermann*, 1996; *Le Provost and Lyard*, 1997; *Egbert and Ray*, 2001]. This energy is mainly dissipated by bottom friction in the shallow ocean areas [*Le Provost and Lyard*, 1997]. Internal tides also play an important role in this dissipation. By using altimeter data, *Egbert and Ray* [2001] have established that about 1/3 of the global ocean tide dissipates in the deep ocean

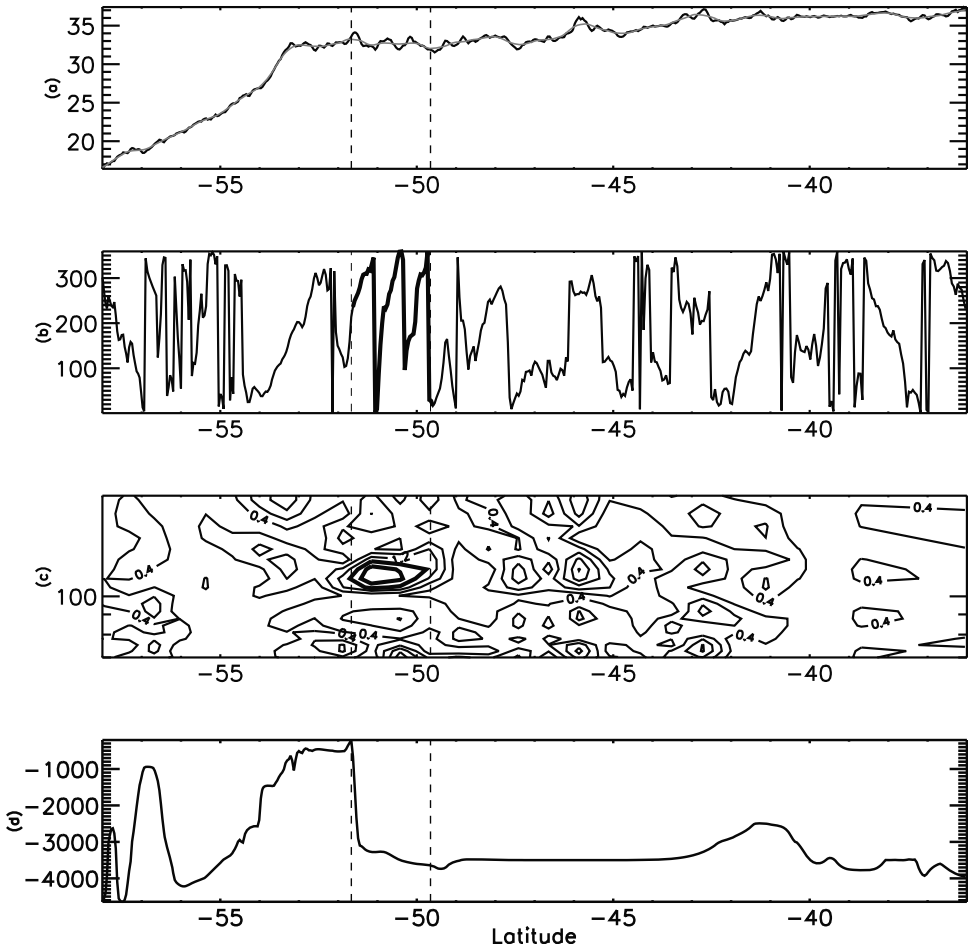

Figure 8. The TP altimeter track 153 (see Figure 9 for the track location): (a) Along-track amplitudes (in cm) deduced from harmonic analysis for the M_2 component (black line) and low-pass filtered amplitudes (gray line). (b) Phase of the residual signal. The bold part of the curve indicates the areas of constantly increasing phase. (c) Short-time Fourier transform of the baroclinic signal. The wavelengths (*y* axis) are in km. Isolines in bold indicate areas where important amplitudes are found for the approximate wavelength of the first M_2 baroclinic mode which is about 100–110 km. (d) Along-track bathymetry (in m). Dashed lines delimit the area of internal tides.

by internal tide generation, agreeing with the estimates of *Sjöberg and Stigebrandt* [1992] and *Kantha and Tierney* [1997] using modeling. By modeling internal tides at the global scale, *Simmons et al.* [2004] obtained a conversation rate from M_2 barotropic tides to M_2 internal tide generation of 0.67 TW using a two layer ocean approximation, and of 0.89 TW for a 10 layer model, similar to the *Egbert and Ray* [2001] estimation. At the regional scale, *Simmons et al.* [2004] provided conversion rates higher than the published estimations in the Hawaii region [*Egbert and Ray*, 2001; *Ray and Cartwright*, 2001; *St. Laurent et al.*, 2003] and higher conversion rates over the Palu ridge [*Egbert and Ray*, 2001]. In the KP region, *Simmons et al.* [2004] estimate energy transfer between 6 GW for the two layer model and 9 GW for the 10 layer model. However, according to the other studies from measurements and regional modeling, these estimates have to be carefully used and are overestimated by a factor of $O(10–100)$ in the region around the South Scotia Ridge [*Padman et al.*, 2006; *Heywood et al.*, 2002]. Thus estimations of *Simmons et al.* [2004] are just considered as an order of magnitude in our study.

[19] We have computed the rate of dissipation from our regional barotropic model parameterization in the KP area. We found a value of 15 GW; that is, ~2% of the global estimation and within a factor of 1.5–2 with the estimate of *Simmons et al.* [2004]. The energy transfer occurs over the southern KP, Elan Bank, and principally over the northern KP, which is consistent with previous model results [*Simmons et al.*, 2004].

[20] From baroclinic elevations derived from altimetry and ocean density profiles, we can estimate the energy dissipated via the internal tide generation process around the KP. We approximated the hydrographic profile shown in Figure 5 as a two-layer stratification with density and depth values of $(\rho_1, h_1) = (1026.3 \text{ kg m}^{-3}, 250 \text{ m})$ and $(\rho_2, h_2) = (1027.7 \text{ kg m}^{-3}, 3000 \text{ m})$. Displacements of the two layers (ξ_1, for the

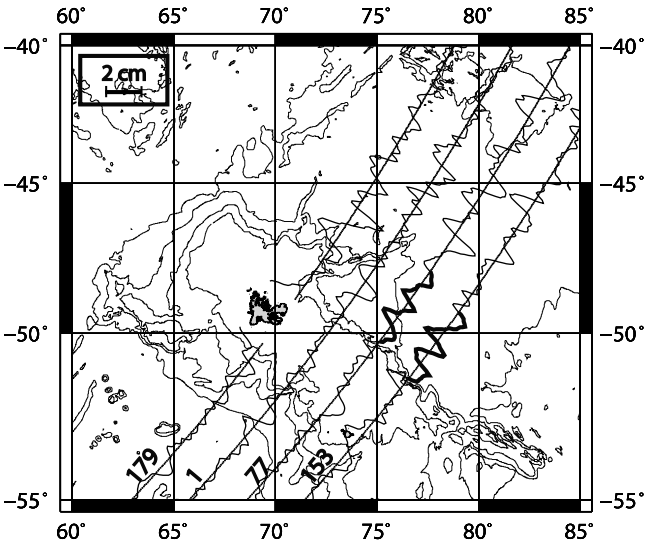

Figure 9. Along-track baroclinic amplitudes (in cm). Altimeter track numbers are indicated. Sections in bold indicate areas of internal tide amplitudes. The bathymetry contours at every 1000 m are overplotted.

free-surface elevations, and ξ_2) are linked by the following relation [*Ray and Mitchum*, 1997]:

$$\frac{\xi_1}{\xi_2} = -\frac{\Delta\rho}{\rho}.$$

From this stratification, the first baroclinic Rossby radius of deformation R_d is defined by: $R_d = \frac{1}{f}\sqrt{g'\frac{h_1 h_2}{h_1+h_2}}$ with $g' = \frac{\Delta\rho}{\rho}g$ is the reduced gravity. We obtain $R_d \approx 17$ km which is consistent with a wavelength of $2\pi R_d \approx 110$ km. The mean square baroclinic amplitudes obtained using altimetric data are $\langle\xi_1^2\rangle = 1.4$ cm^2 over a tidal cycle, thus $\langle\xi_2^2\rangle = 7.7$ m^2. We can compute the mean potential energy density (E) from the internal tide displacements ξ_2 [*Gill*, 1982]. It is a given by:

$$E = \Delta\rho\langle\xi_2^2\rangle.$$

Over the shelf break, we find $E \approx 1000$ J m^{-1}. Knowing E, we can determine the mean energy flux $F = cE$ [*Gill*, 1982], where c is the phase velocity of the wave. Over the M_2 tidal period and the wavelength determined previously, we obtain a mean energy flux of $F \approx 3000$ W m^{-2} directed away from the plateau. East of the northern KP, between Kerguelen Islands and Heard Island, where we have established a clear internal tide signal from altimetry, we find a total energy of 0.81 GW. This value agrees quite well with the estimate of 0.57 GW obtained in our regional barotropic tide model from the parameterization of M_2 barotropic-to-baroclinic energy conversion in the same area.

6. Discussion

[21] Breaking internal gravity waves is a source of mechanical energy that contributes to vertical ocean mixing and tidally driven mixing is one of the major driving mechanisms for maintaining the thermohaline circulation [*Munk and Wunsch*, 1998; *St. Laurent and Garrett*, 2002; *St. Laurent et al.*, 2002]. However, the nature of dissipation and the spatial distribution of mixing are unclear. It is generally admitted that 10% to 30% of the resultant baroclinic tidal energy dissipates locally [*Munk and Wunsch*, 1998; *St. Laurent et al.*, 2002; *Carter et al.*, 2008]: the energy converted into internal tide modes is trapped and then locally dissipated as turbulence close to the generation site. The dominant source of local dissipation and associated mixing is possibly due to high modes [*Polzin et al.*, 1997]. Thus, we can reasonably suggest that some of the M_2 internal tide energy is dissipated near the KP shelf break and is a source of mixing in this region. The other amount of internal tide energy (most of it) radiates away from the inferred generation region in the form of low mode waves [*Polzin et al.*, 1997; *Munk and Wunsch*, 1998; *St. Laurent et al.*, 2002]. We clearly see that part of the first M_2 baroclinic mode energy radiates away from the KP. Figure 8 shows that the coherence of the internal waves is destroyed by the strong ACC currents as the internal waves do not appear again on the other side of the ACC. However, Figure 8c still shows signal for wavelengths of about 110 km but the amplitudes of the signal are clearly reduced north of the ACC. This suggests that most if not all of the energy carried by mode 1 is dumped in the narrow confines of the ACC. The dissipation of the mode 1 energy in the ACC suggests that deep mixing is occurring within this region of enhanced current shear and may contribute to maintain the meridional overturning circulation.

7. Conclusion

[22] This paper has considered the M_2 internal tide signal originating from the northern KP slope. Our barotropic tide model has shown strong cross-slope M_2 energy flux and the model parameterization of internal wave drag energy dissipation suggests that high conversion rates from the barotropic mode to internal tide modes of M_2 occurs in the northern KP region. The possible sites of internal tide generation obtained in the model are consistent with a theoretical criterion [*Baines*, 1986].

[23] To prove the existence of baroclinic tides around the KP, we have analyzed 15 years of TP and Jason-1 radar altimeter repeat-track data. Mode 1 M_2 internal tides are seen as periodic sea surface height signals with amplitudes of $O(1)$ cm and wavelengths of ~110 km, the latter being consistent with values based on the regional stratification [*Chelton et al.*, 1998]. The internal tides are generated at the northern KP slope and propagate northward toward the southern ACC front, at which point coherence drops rapidly. Areas of larger sea surface height variability at the aliased M_2 period (62.1 days) are found in the ACC frontal areas: we associate this signal with mesoscale activity in the ACC.

[24] We have estimated that ~ 0.81 GW was converted from barotropic to baroclinic tidal modes between Kerguelen and Heard Islands. This value is consistent with the estimation of *Kantha and Tierney* [1997], who used a global baroclinic tide model. The parameterized rate of conversion in our barotropic model is also consistent with energetics of internal tides based on our analyses of the altimeter data, providing confidence that the internal wave drag energy dissipation term in the *T-UGO-m* model, is a useful scientific

tool for more detailed explorations of internal tide distribution and dynamics.

[25] On the basis of comparisons with other studies we assume that, while most internal tide energy generated over the KP will radiate away from the region, some fraction will dissipate locally to contribute to mixing in this region. The radiation northward into the ACC may lead to higher dissipation there, and thus contribute to diapycnal mixing in the ACC even well north of internal tide sources. Thus, tidal processes over the KP may be an important driving mechanism to maintain the meridional overturning circulation.

[26] An improvement in the knowledge of baroclinic tides in the KP region will require additional modeling. The next step could be a three-dimensional modeling of internal tide propagation to characterize its time variable component, to better estimate the energy dissipated through internal tide generation around the KP and to study the interactions between the internal waves and the ACC. For these future modeling studies, altimetry data will provide a valuable test of model performance. Furthermore, such analyses allow us to remove the contribution of low-mode baroclinic tides from altimetry, to improve studies longer time processes observed by altimetry.

References

Apel, J. R. (1987), *Principle of Ocean Physics*, 634 pp., Academic, London.

Baines, P. G. (1982), On internal tide generation models, *Deep Sea Res.*, *29*, 307–338, doi:10.1016/0198-0149(82)90098-X.

Baines, P. G. (1986), Internal tides, internal waves and near-internal motion, in *Baroclinic Processes on Continental Shelves*, *Coastal Estuarine Sci.*, vol. 3, edited by N. K. Moores, pp. 19–31, AGU, Washington, D. C.

Carrère, L., and F. Lyard (2003), Modeling the barotropic response of the global ocean to atmospheric wind and pressure forcing: Comparisons with observations, *Geophys. Res. Lett.*, *30*(6), 1275, doi:10.1029/2002GL016473.

Carrère, L., C. Le Provost, and F. Lyard (2004), On the statistical stability of the M_2 barotropic and baroclinic tidal characteristics from along-track TOPEX/Poseidon satellite altimetry analysis, *J. Geophys. Res.*, *109*, C03033, doi:10.1029/2003JC001873.

Carter, G. S., M. A. Merrifield, J. M. Becker, K. Katsumata, M. C. Gregg, D. S. Luther, M. D. Levine, T. J. Boyd, and Y. L. Firing (2008), Energetics of the M_2 barotropic to baroclinic tidal conversion at the Hawaiian Islands, *J. Phys. Oceanogr.*, *38*, 2205–2223, doi:10.1175/2008JPO3860.1.

Cartwright, D. E. (1993), Theory of ocean tides with application to altimetry, in *Satellite Altimetry and Earth Science*, *Lect. Notes Earth Sci. Ser.*, vol. 50, edited by L. Fu and A. Cazenave, pp. 100–141, chap. 6, Academic, San Diego, Calif.

Chelton, D. B., R. A. deSzoeke, M. G. Schlax, K. El Naggar, and N. Siwertz (1998), Geographical variability of the first baroclinic Rossby radius of deformation, *J. Phys. Oceanogr.*, *28*, 433–460, doi:10.1175/1520-0485(1998)028<0433:GVOTFB>2.0.CO;2.

Chiswell, S. M. (1994), Vertical structure of the baroclinic tides in the central North Pacific subtropical gyre, *J. Phys. Oceanogr.*, *24*, 2032–2039, doi:10.1175/1520-0485(1994)24[2032:VSOTBT]2.0.CO;2.

Cummins, P. F., J. Y. Cherniawsky, and M. G. G. Foreman (2001), North Pacific internal tides from the Aleutian Ridge: Altimeter observations and modelling, *J. Mar. Res.*, *59*, 167–191, doi:10.1357/002224001762882628.

Desai, S. D., J. M. Wahr, and Y. Chao (1997), Error analysis of empirical ocean tide models estimated from TOPEX/Poseidon altimetry, *J. Geophys. Res.*, *102*, 25,157–25,172, doi:10.1029/97JC01916.

Dushaw, B. D. (2002), Mapping low-mode internal tides near Hawaii using TOPEX/Poseidon altimeter data, *Geophys. Res. Lett.*, *29*(8), 1250, doi:10.1029/2001GL013944.

Dushaw, B. D., B. D. Cornuelle, P. F. Worcester, B. M. Howe, and D. S. Luther (1995), Barotropic and baroclinic tides in the central North Pacific Ocean determined from long-range reciprocal acoustic transmissions, *J. Phys. Oceanogr.*, *25*, 631–647, doi:10.1175/1520-0485(1995)025<0631:BABTIT>2.0.CO;2.

Egbert, G. D., and R. D. Ray (2001), Estimates of M_2 tidal energy dissipation from TOPEX/Poseidon altimeter data, *J. Geophys. Res.*, *106*, 22,475–22,502, doi:10.1029/2000JC000699.

Egbert, G. D., R. D. Ray, and B. G. Bills (2004), Numerical modeling of the global semidiurnal tide in the present day and in the last glacial maximum, *J. Geophys. Res.*, *109*, C03003, doi:10.1029/2003JC001973.

Gill, A. E. (1982), *Atmosphere-Ocean Dynamics*, *Int. Geophys. Ser.*, vol. 30, 267 pp., Academic, London.

Heywood, K. J., A. C. Naveira Garabato, and D. P. Stevens (2002), High mixing rates in the abyssal Southern Ocean, *Nature*, *415*, 1011–1014, doi:10.1038/4151011a.

Jayne, S. R., and L. C. St. Laurent (2001), Parameterizing tidal dissipation over rough topography, *Geophys. Res. Lett.*, *28*, 811–814, doi:10.1029/2000GL012044.

Kagan, B. A., and J. Sündermann (1996), Dissipation of tidal energy, paleotides, and evolution of the Earth-Moon system, *Adv. Geophys.*, *38*, 179–266, doi:10.1016/S0065-2687(08)60021-7.

Kantha, L. H., and C. C. Tierney (1997), Global baroclinic tides, *Prog. Oceanogr.*, *40*, 163–178, doi:10.1016/S0079-6611(97)00028-1.

Le Provost, C., and F. Lyard (1997), Energetics of the M_2 barotropic ocean tides: An estimate of bottom friction dissipation from a hydrology model, *Prog. Oceanogr.*, *40*, 37–52, doi:10.1016/S0079-6611(97)00022-0.

Llewellyn Smith, S. G., and W. R. Young (2002), Conversion of the barotropic tide, *J. Phys. Oceanogr.*, *32*, 1554–1566, doi:10.1175/1520-0485(2002)032<1554:COTBT>2.0.CO;2.

Lyard, F., F. Lefèvre, T. Letellier, and O. Francis (2006), Modelling the global ocean tides: Modern insight from FES2004, *Ocean Dyn.*, *56*, 394–415, doi:10.1007/s10236-006-0086-x.

Maraldi, C., B. Galton-Fenzi, F. Lyard, L. Testut, and R. Coleman (2007), Barotropic tides of the Southern Indian Ocean and the Amery Ice Shelf cavity, *Geophys. Res. Lett.*, *34*, L18602, doi:10.1029/2007GL030900.

Mitchum, G. T., and S. M. Chiswell (2000), Coherence of internal tide modulations along the Hawaiian ridge, *J. Geophys. Res.*, *105*, 28,653–28,661, doi:10.1029/2000JC900140.

Morozov, E. G. (1995), Semidiurnal internal wave global field, *Deep Sea Res. Part I*, *42*, 135–148, doi:10.1016/0967-0637(95)92886-C.

Munk, W., and C. Wunsch (1998), Abyssal recipes II: Energetics of tidal and wind mixing, *Deep Sea Res. Part I*, *45*, 1977–2010, doi:10.1016/S0967-0637(98)00070-3.

Padman, L., S. Howard, and R. Muench (2006), Internal tide generation along the South Scotia Ridge, *Deep Sea Res. Part II*, *53*, 157–171, doi:10.1016/j.dsr2.2005.07.011.

Park, Y.-H., L. Gamberoni, and E. Charriaud (1993), Frontal structure, water masses, and circulation in the Crozet Basin, *J. Geophys. Res.*, *98*, 12,361–12,385, doi:10.1029/93JC00938.

Park, Y.-H., E. Charriaud, and M. Fieux (1998), Thermohaline structure of the Antarctic surface water/winter water in the Indian sector of the Southern Ocean, *J. Mar. Syst.*, *17*, 5–23, doi:10.1016/S0924-7963(98)00026-8.

Parke, M. E., R. H. Stewart, D. L. Farless, and D. E. Cartwright (1987), On the choice of orbits for an altimetric satellite to study ocean circulation and tides, *J. Geophys. Res.*, *92*, 11,693–11,707, doi:10.1029/JC092iC11p11693.

Pingree, R. D., and A. L. New (1989), Downward propagation of internal tidal energy into the Bay of Biscay, *Deep Sea Res. Part A*, *56*, 735–758.

Polzin, K. L., J. M. Toole, J. R. Ledwell, and R. W. Schmitt (1997), Spatial variability of turbulent mixing in the abyssal ocean, *Science*, *276*, 93–96, doi:10.1126/science.276.5309.93.

Ray, R. D., and D. E. Cartwright (2001), Estimates of internal tide energy fluxes from TOPEX/Poseidon altimetry: Central North Pacific, *Geophys. Res. Lett.*, *28*, 1259–1262, doi:10.1029/2000GL012447.

Ray, R. D., and G. T. Mitchum (1996), Surface manifestation of internal tides generated near Hawaii, *Geophys. Res. Lett.*, *23*, 2101–2104, doi:10.1029/96GL02050.

Ray, R. D., and G. T. Mitchum (1997), Surface manifestation of internal tides in the deep ocean: Observations from altimetry and island gauges, *Prog. Oceanogr.*, *40*, 135–162, doi:10.1016/S0079-6611(97)00025-6.

Roblou, L., F. Lyard, M. Le Henaff, and C. Maraldi (2006), X-TRACK: A new processing tool for altimetry in coastal oceans, paper presented at Symposium on 15 Years of Progress in Radar Altimetry, Eur. Space Agency, Venice, Italy, 13–18 Mar.

Siedler, G., and U. Paul (1991), Barotropic and baroclinic tidal currents in the eastern basins of the North Atlantic, *J. Geophys. Res.*, *96*, 22,259–22,271, doi:10.1029/91JC02319.

Simmons, H. L., R. W. Hallberg, and B. K. Arbic (2004), Internal wave generation in a global baroclinic tide model, *Deep Sea Res. Part II*, *51*, 3043–3068, doi:10.1016/j.dsr2.2004.09.015.

Sjöberg, B., and A. Stigebrandt (1992), Computations of the geographical distribution of the energy flux to mixing processes via internal tides and associated vertical circulation in the ocean, *Deep Sea Res.*, *39*, 269–291, doi:10.1016/0198-0149(92)90109-7.

St. Laurent, L., and C. Garrett (2002), The role of internal tides in mixing the deep ocean, *J. Phys. Oceanogr.*, *32*, 2882–2899, doi:10.1175/1520-0485(2002)032<2882:TROITI>2.0.CO;2.

St. Laurent, L. C., H. L. Simmons, and S. R. Jayne (2002), Estimating tidally driven mixing in the deep ocean, *Geophys. Res. Lett.*, *29*(23), 2106, doi:10.1029/2002GL015633.

St. Laurent, L. C., S. Stringer, C. Garrett, and D. Perrault-Joncas (2003), The generation of internal tides at abrupt topography, *Deep Sea Res. Part I*, *112*, 457–467.

Tierney, C., M. E. Parke, and G. H. Born (1998), An investigation of ocean tides derived from along-track altimetry, *J. Geophys. Res.*, *103*, 10,273–10,287, doi:10.1029/98JC00448.

Vlasenko, V. I., and Y. G. Morozov (1993), Generation of semidiurnal internal waves near the submarine ridge, *Oceanology*, *33*, 282–286.

Vlasenko, V., N. Stashchuk, and K. Hutter (2005), *Baroclinic Tides*, Cambridge Univ. Press, New York, doi:10.1017/CBO9780511535932.

R. Coleman, Antarctic Climate and Ecosystems CRC, Private Bag 80, Hobart, Tas 7001 Australia.

F. Lyard and L. Testut, Laboratoire d'Etudes en Géophysique et Océanographie Spatiales, CNRS, 14 Ave. Edouard Belin, Toulouse F-31400, France.

C. Maraldi (corresponding author), Service Hydrographique et Océanographique de la Marine, 42 Ave. Gaspard Coriolis, F-31057 Toulouse CEDEX, France. (claire.maraldi@gmail.com)